Shock Waves (2015) 25:239–254
DOI 10.1007/s00193-014-0525-4

ORIGINAL ARTICLE

# Large-scale spray detonation and related particle jetting instability phenomenon

**F. Zhang · R. C. Ripley · A. Yoshinaka · C. R. Findlay · J. Anderson · B. von Rosen**

Received: 26 October 2013 / Revised: 30 July 2014 / Accepted: 27 August 2014 / Published online: 9 October 2014


**Abstract** The detonation performance of a more than 70,000 $m^3$ fuel spray-air cloud is experimentally investigated using dispersal of a 5,090 kg gasoline payload by a central explosive in a cylindrically stratified configuration. The large-scale explosive dispersal data are further analyzed, together with a revisit of the data from previously conducted small-scale experiments and numerical simulations, to study particle jetting instabilities. The experiments depict a dual hierarchical jet structure consisting of primary particle jets overlapped by fine particle jets on the primary surfaces. Both jet systems form within the expansion of 1.5–2 times the initial charge diameter. The fine droplet jets are numerous initially as a result of surface instabilities or fragmentation of the charge casing, while the primary jets have a limited number emerging out of the surface of fine jet structures later in time. The number of primary jets is consistent with the number of incipient radial fractures observed at the payload surface. From this fact, an instability mechanism is suggested that the formation of primary particle jets may originate in the perturbations that develop near the interior interface between explosive and payload, through non-uniform density effects or casing fragmentation, driven by the explosive detonation and subsequent expansion of the high-pressure detonation products. Numerical modeling using liquid payload fragmenting into droplet particles has been applied to investigate the proposed mechanism. The numerical results show that the high-pressure jets of detonation products, created from the interior casing fragmentation, radially fracture the payload. The resulting compressed radial filaments, developed within the payload, lead to the primary jets emerging between the radial fracture points at the payload surface. The number of interior payload filaments before payload surface bursting, and hence the number of primary jets, is controlled by the number of inner casing fragments at the explosive-payload interface. Furthermore, the number of primary jets is also influenced by the mass ratio of payload to explosive and inner casing fragment pattern, whereas the perturbations induced by minor fragments will dissipate through the large payload and not result in final filaments.

**Keywords** Spray detonation · Multiphase flow · Heterogeneous explosive · Interface instability · Particle clustering · Particle jets

Communicated by G. Ciccarelli.

This paper is based on work that was presented at the 24th International Colloquium on the Dynamics of Explosions and Reactive Systems, Taipei, Taiwan, July 28 - August 2, 2013.

F. Zhang (✉) · A. Yoshinaka · C. R. Findlay · J. Anderson
Defence R&D Canada—Suffield, P.O. Box 4000, Medicine Hat, AB T1A 8K6, Canada
e-mail: fan.zhang@drdc-rddc.gc.ca

R. C. Ripley
Martec Limited, 1888 Brunswick St., Suite 400, Halifax, NS B3B 3J8, Canada
e-mail: robert.ripley@lr.org

B. von Rosen
Canadian Explosives Research Laboratory, 1 Haanel Drive, Ottawa, ON K1A 1M1, Canada
e-mail: bert.vonrosen@nrcan-rncan.gc.ca

## 1 Introduction

Large-scale experiments on unconfined detonation of motor fuel sprays or solid particles in air provide valuable fundamental data. Such phenomena, for instance, were reported by Alekseev et al. [1,2] for semi-cylindrical clouds of gasoline or kerosene spray, 1,100–1,500 $m^3$ in volume and 3–8 m in radius; in explosively dispersed spray clouds from

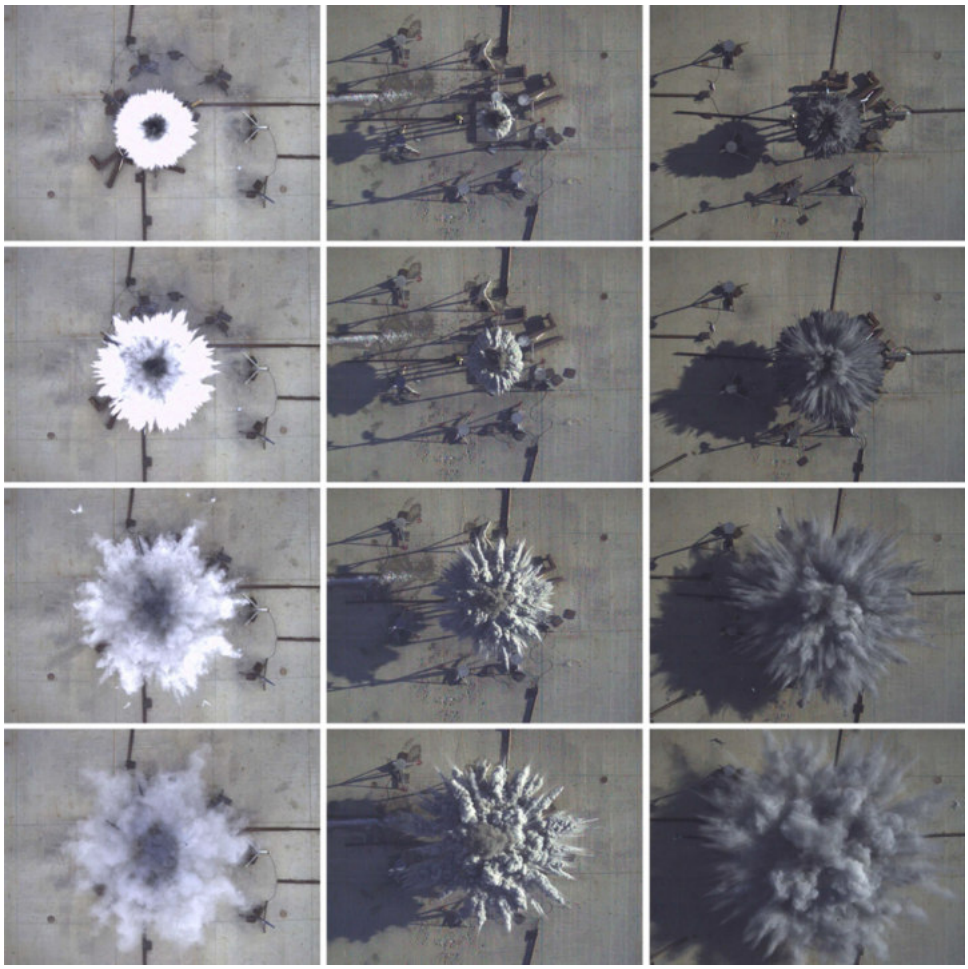

**Fig. 1** Explosive dispersal of a 114 mm dia. cylindrical charge that consists of an explosive in a central glass tube surrounded by an annular payload. *Left* liquid alone (# U04281B); *middle* dry Al particles alone (# U04328B); and *right* an Al particle-liquid hybrid mixture (# U04308A). Timings from *top to bottom* are 5, 10, 25, and 50 ms [8]

a gasoline, kerosene or diesel fuel canister weighing 0.1–100 metric tons [3,4]; and reported by Zhang et al. [5] for a quarter-cylindrical cloud of aluminum particles, 230 $m^3$ in volume and 4 m in radius. The results show that the gasoline spray, after a sufficiently long suspension time, requires a critical TNT charge mass of 0.64 kg to initiate detonation [1,2]. As the suspension time is reduced, the critical initiation charge mass increases to a few kilograms. The critical initiation charge mass is 4.5 kg for kerosene spray detonation [1] and 5–8 kg for flake and 2–3 μm atomized aluminum-air detonation [5]. The critical blast radius is reported to be $R_C = 2.75\,\text{m} \approx 55\,\lambda$ for gasoline-air in long-time suspension [2] and $R_C = 10\,\text{m} \approx 20\,\lambda$ for aluminum-air, where $\lambda$ is the detonation cell width [5]. The smaller critical initiation charge mass and detonation cell width for gasoline indicates that its detonation, after a sufficiently long spray suspension time, is controlled by the vapour phase. The fact that gasoline spray in short-time suspension and kerosene spray require the same order of critical initiation charge mass as that of aluminum particles suggests the dominance of liquid droplets in heterogeneous detonation of low vapour pressure fuels.

The performance of detonation is dictated by both concentration and shape of the fuel cloud. When a liquid or a packed bed of metallic particles is explosively dispersed, incipient perturbations develop visibly on the surface of the cloud. At higher dispersal speeds, the droplet or particle cloud is highly perturbed and coherent jet structures form during the expansion (see Fig. 1) [6–14]. The formation of particle clusters and jets is widely observed in nature, with examples such as supernovae, volcanic eruptions, embedded landmine explosions and shallow underwater explosions. Explosive dispersal is a potentially effective research approach to gain insights into this universal instability phenomenon.

While the phenomenon has been extensively observed, the physical mechanisms behind clustering and jetting instabilities and their associated multiphase simulations remain a significant challenge. Milne et al. [9] pointed out that the Rayleigh–Taylor instability, which takes a long time to develop, was unlikely the cause of the formation of jet structures. Yet it is unclear if the early phase of the shock-induced Rayleigh–Taylor instability, often called Richtmyer–Meshkov instability resulting from a detonation shock crossing the explosive boundary in this case, can attract the

particles and affect their jetting formation. Frost et al. [10] postulated that the breakup of a layer of particles at high strain rates was governed by a balance of expansion inertia effects tending to fracture the layer versus viscous dissipation which tends to maintain the stability of the layer. An analysis of experimental data from cylindrical explosive dispersal of both bulk liquid and granular solids indicates that the incipient number of particle jets was associated with the initial particle expansion velocity [11]. The experimental initial particle expansion velocity was found to be related to the so-called "Gurney velocity", which is determined from both the explosion energy and mass ratio of dispersal payload to explosive. Through meso-scale simulations Xu et al. [12,13] indicated that micro-jets of detonation products are developed due to the non-uniform density effect at the multiphase interface between the center explosive and the surrounding packed particle bed; this could lead to one of the origins of jetting formation.

It is clear that explosive dispersal of granular materials, as compared with bulk liquid dispersal, will introduce additional physical effects due to their discrete solid nature, such as initial particle morphology and size distribution, initial particle bed packing configuration and subsequent dynamic compaction, as well as shock sintering and melting phase transition. However, instabilities from non-uniform density effects near the interface, driven by explosive detonation and the subsequent expansion, and their interactions with bulk deformable and compressible materials may still significantly contribute to the jetting phenomenon in both liquid and granular material dispersal. Perhaps a thorough understanding of bulk material dispersal would be the first step before accounting for the complicated effects from the grain-scale physics of discrete solid systems. Large-scale experiments would also be necessary to distinguish instability origins from such complex phenomena with the required resolution, which has been difficult in small-scale experiments.

In the present paper, the dispersal and subsequent detonation of a large-scale unconfined gasoline spray of more than 70,000 $m^3$ has been experimentally investigated to examine both detonation performance and scale effect. The large-scale dispersal data are further analyzed, together with a revisit of the data from previously conducted small-scale experiments and numerical simulations, in order to explore new knowledge in particle jetting instabilities relevant to a payload packed in a stratified shell surrounding an explosive.

## 2 Large-scale spray detonation

### 2.1 Experimental methodology

The detonation experiment was carried out in an explosively dispersed spray cloud from a fuel canister configuration; 7,100 litres of gasoline (clear primary without ethanol supplied by Petro Canada) was contained within a polyethylene-walled cylindrical container, 1.6 m in inner diameter. The density of gasoline was measured to be 0.717 g/$cm^3$ which resulted in a total test fuel weight of 5,090 kg. The gasoline was dispersed using a centrally located cylindrical explosive burster charge contained within a thin-walled hard PVC tube, where this charge was detonated from the top with an exploding wire RP83 detonator (0.08 g PETN plus 1.031 g RDX). The primary gasoline charge had a 5.75 m height of burst which is defined as the distance from charge center to ground level.

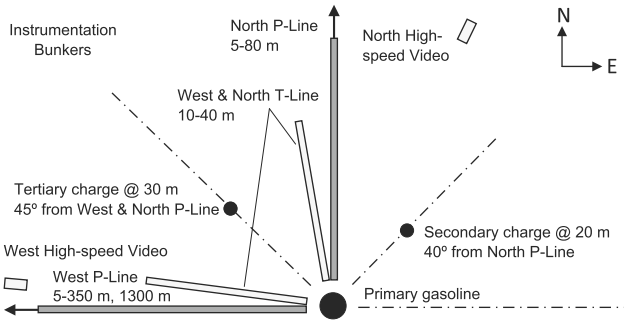


**Fig. 2** Schematic of test set-up

In order to directly initiate the detonation of dispersed gasoline spray, a secondary charge was used with a mass greater than the critical initiation charge mass defined in [1,2]. It was located at a radius $R = 20$ m from the gasoline canister at 40° clockwise from the north P-line of pressure transducers as schematically shown in Fig. 2. The location of the secondary charge avoided its unintentional initiation by the primary charge dispersal and related fragment impact. An additional tertiary charge with the same mass was placed at $R = 30$ m from the gasoline canister at 45° between the west and north P-lines. The tertiary charge ensured the direct initiation of spray detonation in case the secondary charge failed. Both secondary and tertiary charges had a height of burst of 1.5 m, initiated from the top using an RP83 detonator.

Pressures and impulses were measured using ground level rail-style gauge mounts with Endevco 8530 piezo-resistive transducers, which were located (in meters) at 5.5, 8, 10.5, 13, 15.5, 18, 20.5, 23, 25.5, 28, 38, 43, 48, 53, 60, 70, 80, 120, 160, 200 and 350 from the primary gasoline charge center in the west radial P-line and at 5, 10, 15, 18, 19, 20, 21, 22, 30, 40, 50, 60, 70 and 80 in the north radial P-line (Fig. 2). In addition, PCB piezo-electric transducers were installed at 1,297 m west of the gasoline charge center using one ground-level mount and one side-on "lollipop"-style gauge mount. Flame temperatures were measured using Omega C-Type thermocouples (calibrated up to 2, 200 °C) which were made of a 5 mm long section of twisted tungsten and rhenium wires with a bundle diameter of 0.127 mm. The thermocouples have a slow response time, on the order of milliseconds, and


**Fig. 3** Photographs before and after detonation of dispersed gasoline spray cloud

therefore provide a history of ms-averaged fireball temperature. A series of thermocouples were installed on 1.5 m high stands and separated in intervals of 4–5 m along the west radial T-line and the north radial T-line from the gasoline charge center as sketched in Fig. 2. The radial alignment of P-lines and T-lines in a 5 ° angle separation minimized the influence of gauge mounts on the measurements. High-speed video cameras were employed to record the geometry and process of the event and were mounted along both western and northern directions.

The overall radial gauge alignment was designed for a series of center-initiated large-scale explosion trials. While these existing gauge locations were not ideally aligned with the direction of detonation propagation for this specific gasoline test, they still covered the estimated radius of the spray cloud to provide the values for detonation performance.

The gasoline spray-air mixture was prepared through explosive dispersal using a centrally located cylindrical explosive burster charge. As shown in the photographs in Fig. 3 taken from the near-west high-speed video, detonation of the burster charge caused the gasoline liquid to disperse and formed jets spreading outwards. The beginning of the liquid fuel evaporation was identified through a temperature drop about 15–20 °C in the thermocouple records. The fuel vapor phase is visible in the first photo and is filling the air gaps between the evaporating jets, which now move outwards much slower than the liquid-phase jets during early dispersal. Note that the top vertical black plume in the photo comprises the detonation products from the central burster explosive. At this time, the secondary and tertiary charges are simultaneously detonated and both lead to a direct initiation of detonation of the spray cloud. The second photo in

Fig. 3 shows the blast comprising a leading shock front followed by the fireball later in time after the successful cloud detonation, where the shock front is visible in the cloudy sky background on the left of the photo.

The spray cloud radius (from charge center to jet edge) and height were measured from high-speed photography records (2,000 frames/s). The mean cloud radius and height were averaged from the values of the north and the south jets. Immediately prior to detonation, the cloud radius and height were obtained to be $R = 43.3$ m and $H = 12.7$ m, thus resulting in a cloud volume $\pi R^2 H = 74{,}766\text{m}^3$. Primary gasoline is typically composed of iso-octane, heptane, cyclopentane, ethyl-benzene and butane. Assuming that the total mass of the gasoline was made of iso-octane, at the local air pressure of 92.5 kPa and temperature of 28 °C, the volume for the stoichiometric fuel-air mixture would occupy 71,570 $\text{m}^3$ if the fuel remains in full liquid form and 72,777 $\text{m}^3$ if the fuel is in the full vapor phase. Using a surface evaporation rate of gasoline [15], the evaporated fuel is estimated to be 62 % by mass, in which the surface area also includes the side surfaces of primary fuel jets. The dynamic explosive dispersal during the test could further influence the evaporation rate. The experimental cloud volume 74,766 $\text{m}^3$ divided by the volume of a stoichiometric fuel-air mixture, with 62 % fuel vapor and 38 % fuel liquid by mass, equals $r = 1.034$. Noticing the air gaps between the fuel spray jets at the larger radii in the experiment as shown in Fig. 3, the real experimental volume shall be smaller than that estimated by $\pi R^2 H$, thus shifting the $r$-value towards unity or smaller. An approximately stoichiometric or slightly rich fuel-air mixture on average is therefore preserved when the cloud is detonated.

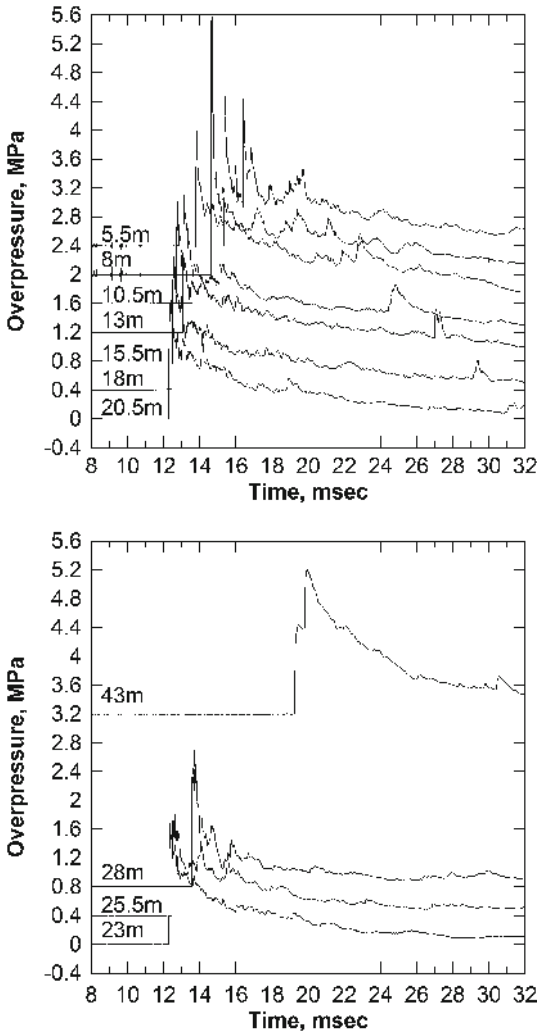


**Fig. 4** Overpressure histories at gauges in the west radial P-line

## 2.2 Detonation results

Figure 4 shows overpressure histories on the ground along the west radial P-line, where the front peak overpressure has a range of $\Delta p = 1.57$–$2.17$ MPa (i.e., a pressure ratio range of $p/p_0 = 18.0$–$24.5$) except for 3.86 MPa at $R = 8$ m. The violent pressure traces are representative for detonation with an exception at $R = 43$ m, where the trace is relatively smooth likely recording the wave in the air gap beneath the cloud edge (see Fig. 3 where the middle of the front view faces the west P-line). The wave arrival times at different locations, with respect to the detonation initiation instant, indicate a partial spherical detonation front propagating nearly from north to south. This detonation is initiated from the tertiary charge at $R = 30$ m, 45 ° between the west and north P-lines (as sketched in Fig. 2), and arrives at the west P-line first at the point between $R = 20.5$ and 23 m.

Figure 5 provides overpressure histories on the ground along the north radial P-line, with a front peak overpressure range of $\Delta p = 1.66$–$2.13$ MPa (i.e., $p/p_0 = 18.9$–$24.0$). The wave arrival times at different locations of the north P-line specify another spherical detonation front, propagating approximately from east to west, initiated from the secondary charge at $R = 20$ m, 40 ° from the north P-line in the clockwise direction (see Fig. 2). While collisions of transverse waves in a three-dimensional detonation front will result in a very high pressure, the front pressure of 3.86 MPa at $R = 8$ m on the west P-line in Fig. 4 is likely produced through collision of the two detonation fronts initiated by the secondary and tertiary charges. Reflection from this wave collision can be traced downstream in the pressure histories of other locations of the west P-line, for example at $R = 5.5$ m. Similarly, the collision of the two spherical detonation fronts near the north P-line can be identified through the reflection waves in the transducers located along the north P-line in Fig. 5. Note that in the pressure trace at $R = 30$ m on the north P-line, there is an abnormally high and wide spike following the front peak, possibly produced by fragment or debris impact. The pressure signal at $R = 40$ m north was

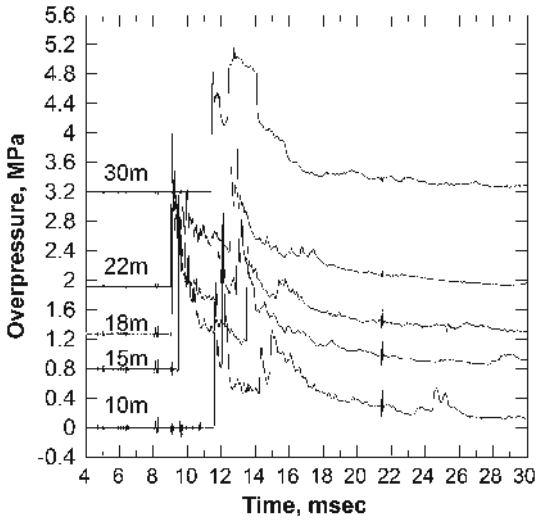


**Fig. 5** Overpressure histories at gauges in the north radial P-line

damaged immediately after the front peak and therefore not shown here.

Detonation velocity has been estimated to avoid the influence of initiation sources (both secondary and tertiary charge). For this purpose, the distance between the west P-line and near the south edge of the cloud is selected. The west P-line has a normal distance of 21.2 m from the tertiary charge and this normal intersection point is further away from the secondary charge (see Fig. 2), whereby the south edge is at the far end of the cloud from both initiation sources. The pressure records at 20.5 and 23 m of the west P-line shown in Fig. 4 provide the pressure profiles for the start point of this selected distance. Both show a normal detonation behavior with a detonation front ($p/p_0 = 18.8$ and 19.7, respectively) followed by a Taylor expansion wave. From the high speed video records, the detonation velocity has been calculated with a mean value of 1,890 m/s over this selected 30 m distance.

Figure 6 summarizes the wave front peak overpressure and maximum impulse at all ground-level gauges along both the west and north P-lines. The overpressure and impulse profiles show a plateau with values mostly in the range of 1.57–2.17 MPa (or $p/p_0 = 18.0$–24.5) and 7.26–13.3 MPa-ms, respectively. This plateau indicates a detonation area with a radius of 40–43 m, in agreement with the high-speed video result ($R \approx 43$ m). An exceptional point is at $R = 38$ m on the west P-line, whereby a peak overpressure of 0.6 MPa is measured likely in the radial air gap between the two primary cloud jets (see Fig. 3 where the middle of the front view faces the west P-line). The high overpressure of 3.86 MPa at $R = 8$ m on the west P-line is not included in Fig. 6, since it is possibly caused by the wave collision rather than the detonation value itself. In Fig. 6, the overpressure and impulse values versus radius after the detonation plateau display the performance of the decaying blast wave up to 1.3 km (about 30 cloud radii).

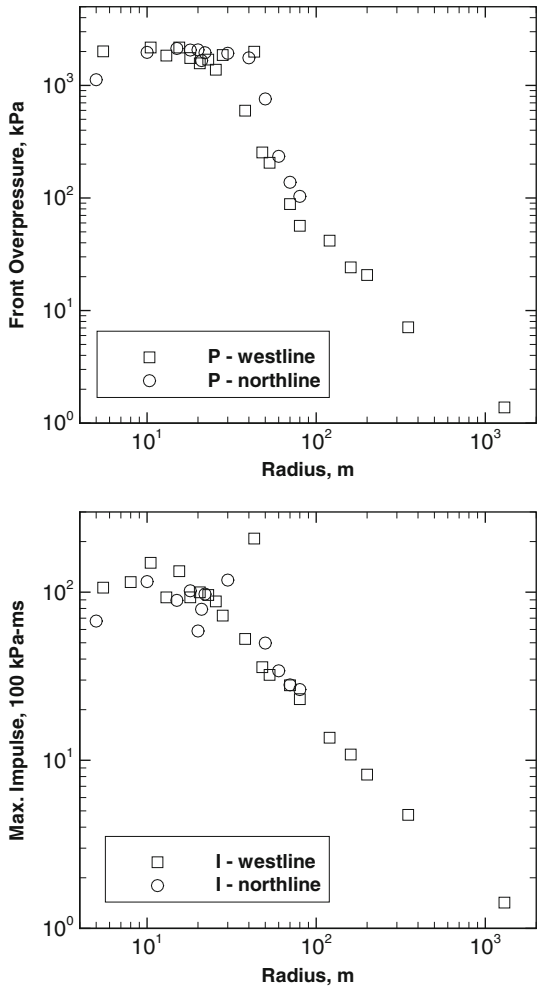


**Fig. 6** Front overpressure and maximum impulse of gasoline spray detonation and subsequent blast

In the literature Alekseev et al. [1,2], measured a detonation velocity between 1,500 and 1,800 m/s and overpressures between 1.5 and 1.8 MPa. Both the detonation velocity and overpressure in the present study are higher. Equilibrium calculations for the Chapman–Jouguet (CJ) detonation have been performed using the Cheetah code from the Lawrence Livermore National Laboratory [16]. The total mass of the gasoline was assumed to be made of iso-octane in the vapor phase and uniformly mixed with air over a range of equivalence ratio, at the local pressure of 92.5 kPa and temperature of 28 °C. The maximum CJ-to-initial pressure ratio is 18.7 with a detonation velocity of 1,810 m/s at the equivalence ratio of 1.15. A real detonation has a three-dimensional wave front, where collisions of transverse waves can cause a pressure far more than twice of the CJ pressure particularly for a multiphase detonation [5]. On the other hand, commercial pressure transducers commonly measure an average pressure resulting from the wave front crossing the transducer surface diameter (3 mm for the Endevco transducers used in this


**Fig. 7** A fine-soiled particle ground record produced by gasoline spray detonation propagating from left to right (*left*) and the authors' interpretation of the cellular structure (*right*)

study). Considering these two reasons, the measured range of peak-to-initial pressure ratio of 18.0–24.5 is very reasonable under the conditions of a partial spray and complicated gasoline composition.

As for the cellular structure of detonation, smoke foils each made of a 2.44 × 1.22 m aluminum sheet were also installed at the ground level. Records, however, were unsuccessful due to liquid spray dispersal and sandy blast winds; the foils were also damaged by the large-scale strong detonation and blast waves. Instead, the cellular structure of the gasoline spray detonation in this study was traced on a large arc area of the ground soil surface, located between the west P-line and the 45 ° north-west line towards the instrumentation bunker and between two radii $R = 3$ and 15 m from the primary charge center (see Fig. 2). The ground surface featured a 10–20 mm thick layer of dry, fine prairie soil particles mostly sub-millimeter in size. This layer was produced through soil deposit from instrumentation cable trenching along the north-west line and further crushed to fine particles by a series of center-initiated large-scale explosion trials prior to the current gasoline trial. Figure 7 provides an example of such records with the authors' interpretation of the cellular structure. The measured average detonation cell width from the records on the arc area is about 7 cm. This result appears to be in agreement with the original records by Alekseev et al. ($\lambda = 3.6 - 10$ cm measured from three smoke foils in [2]), and with the cell widths ($\lambda = 5.4 - 6.74$ cm) measured by Knystautas et al. [17] for stoichiometric alkane gas ($C_2H_6$, $C_3H_8$ or $C_4H_{10}$) fuel-air mixtures in laboratory detonation tubes.

Figure 8 shows a typical temperature history measured with thermocouples. Because of the slow response time of thermocouples, the measured temperatures shall be interpreted as the fireball temperatures later in time after the detonation. The peak fireball temperatures recorded by all thermocouple gauges along both west and north T-lines range between 1,400 and 1,650 K.

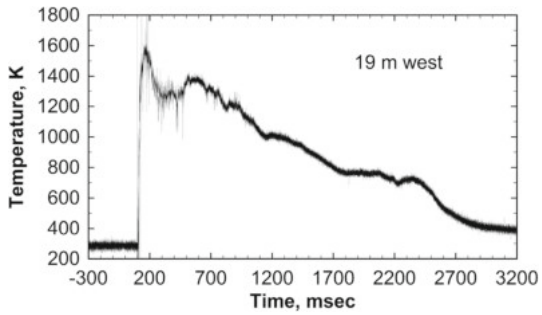


**Fig. 8** A fireball temperature history at thermocouple 19 m in the west radial T-line

## 3 Jetting instabilities of particles

### 3.1 Small-scale experimental observation

Under high speed explosive dispersal, the surface of bulk liquid or a packed bed of solid particles develops high perturbations and coherent jet structures form beginning at very early times, as for example in Fig. 1 where from left to right the payload comprised a pure liquid, dry atomized aluminum particles and a hybrid mixture of both, respectively. The two Litre (L) cylindrical charge configuration used for the three payloads was the same. It consists of a 10 mm diameter cylindrical burster of explosive packed in a central glass tube surrounded by an annular payload contained in a 114 mm diameter, thin-walled polyethylene cylindrical casing. The current study mainly focuses on the primary effect of bulk material behavior on jetting phenomenon; insights into grain-scaled physics are beyond the scope of this work. The liquid payload is therefore selected for further analysis.

The early edge or jet expansion velocity is measured from the video data of the 2 L charges in a range of burster explosive mass, $C$, and payload mass, $M$. The measured jet expansion velocity, $V_j$, is compared to the Gurney velocity, $V_g$, in Fig. 9. The Gurney velocity was introduced for a metal-

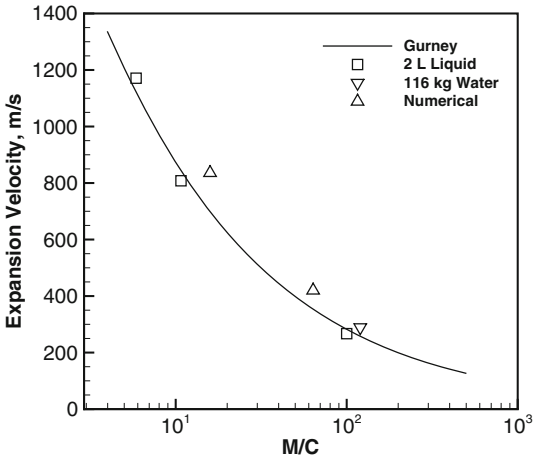


**Fig. 9** Experimental expansion velocities compared to the Gurney velocity theory in a range of mass ratio of liquid payload to explosive

cased explosive charge and describes the maximum expansion velocity of the casing after the charge has detonated. The Gurney velocity is a function of detonation energy, $E_g$, and mass ratio of metal casing to explosive, *M/C*. The formulations of the Gurney velocity for various geometric charges can be found in text books, for example, in [18]. For a cylindrical charge:

$$V_g = \sqrt{2E_g}\,(M/C + 1/2)^{-1/2} \tag{1}$$

Here, the concept of Gurney velocity is extended for a payload such as a liquid or granular material packed in a stratified shell surrounding an explosive, where the traditional casing mass is replaced by the payload mass. Figure 9 also includes the data from a large-scale experiment and numerical calculations to be discussed in Sect. 3.3. The comparisons show that the Gurney velocity agrees well with the incipient jet expansion velocity from both experiments and detailed numerical simulations in a wide range of payload mass. This indicates that detonation energy and *M/C* are key parameters for dispersal.

In order to correlate the initial number of jets with the local conditions at the edge of the charge including a casing, the energy-governed dynamic fragmentation theory by Grady for expanding shells is used for a nominal fragment width, $S$ [19,20]:

$$S = \left(12K_f^2/E\rho\dot{\varepsilon}^2\right)^{1/3} \tag{2}$$

Here, $\dot{\varepsilon}$ is the circumferential strain rate; $K_f$, $\rho$ and $E$ are casing dynamic fracture toughness, material density and elastic modulus, respectively. The results from equation (2) are summarized in Table 1 using strain rate models based on the expansion velocity (i.e., the Gurney velocity) and the sound speed scale, where $P$ and $\rho$ are the post-shocked pressure and density at the charge edge. Comparison with the experimental initial jet number shows the same trend, thus indicating that the initial number of jets may be associated with the fragmentation of the payload casing.

By careful examination of the jet structures from videos for tests using various burster diameters (e.g., Fig. 1), two overlapping jet scales may exist: fine jets and primary jets. The large amount of fine jets appear initially on the surface as the charge casing fragments, while the primary jets may emerge later in time in a more limited number that remains more or less constant. Figure 10 provides the zoom-in photographs from the liquid test in Fig. 1 and it may indicate the emerging time of a primary jet out of the edge of fine jets. The resolution of the small-scale experiments, however, is insufficient to distinguish the phenomenon any further. As listed in Table 1, the number of primary jets increases with burster diameter, that is, with a decrease in mass ratio *M/C* for the 2 L charge configuration.

### 3.2 The mechanism

The phenomenology from the small-scale experiments may be summarized in two aspects. Firstly, a large number of fine jets form very early on the charge surface where the initial jet number appears to be likely related to the fragmentation of the charge surface following the fragmentation theory. Secondly, the number of fine jets decreases in later times likely through aerodynamic interactions, while primary jets seem to appear later in a more coherent structure and their number remains approximately constant. Aerodynamic interaction can help shape jets, but does not explain the number

**Table 1** Number of initial jets compared to theoretical outer case fragmentation calculations

| Configuration | | Experiment | | Theoretical | |
|---|---|---|---|---|---|
| | | | | $\dot{\varepsilon} = V_g/R_0$ | $\dot{\varepsilon} = \sqrt{P/\rho}/R_0$ |
| Trial | Burster (mm) | Number of primary jets | Number of initial jets | Number of case fragments | |
| U04281B | 10 | 9 | 84 | 74 | 80 |
| U04239A | 31 | 13 | 107 | 145 | 121 |
| U04238A | 44 | 16 | 123 | 186 | 133 |

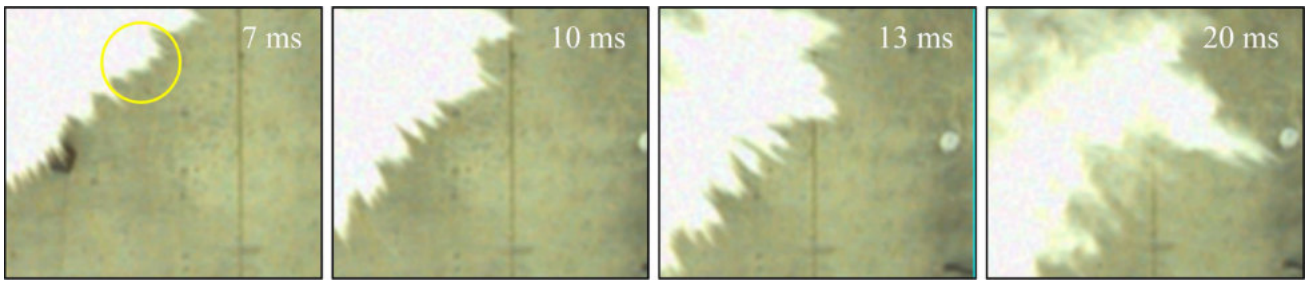


**Fig. 10** Zoom-in photographs showing the emerging of primary jets for the 114 mm dia. liquid charge (# U04281B)

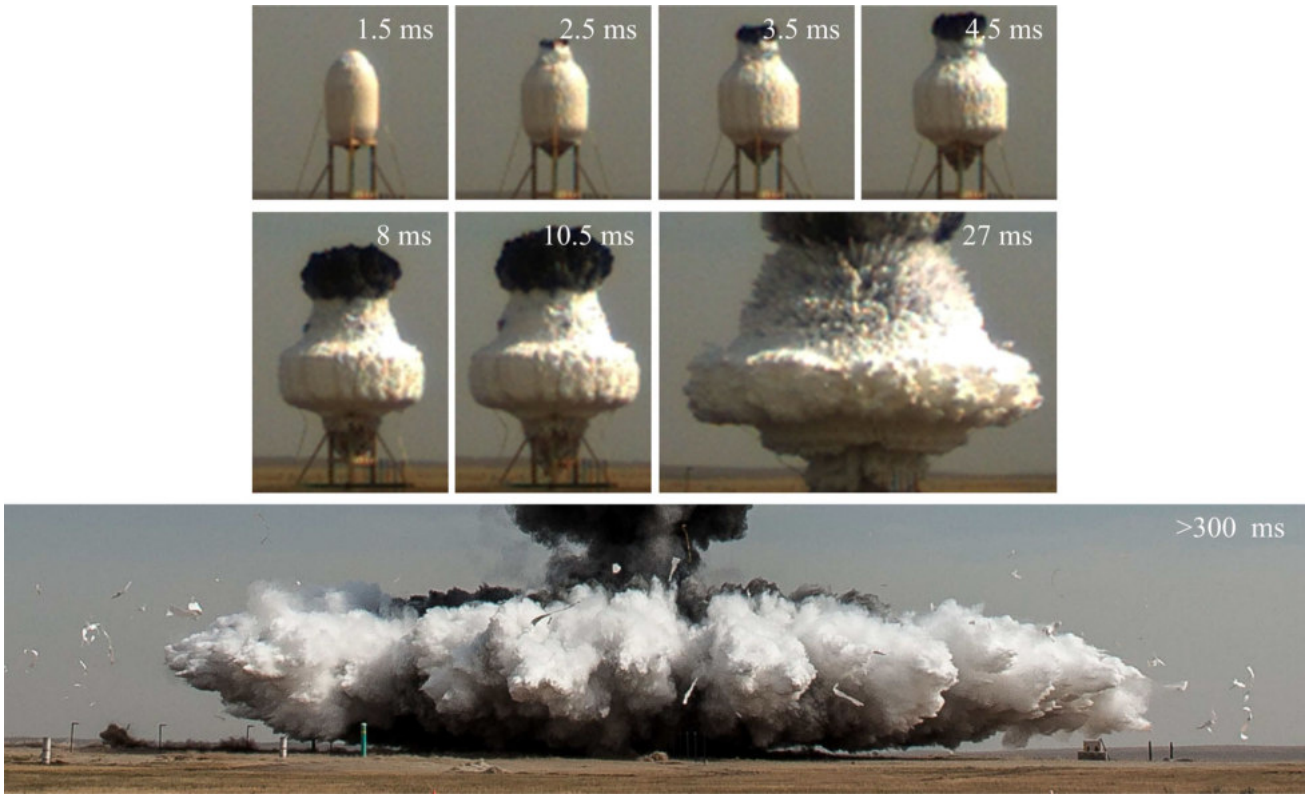


**Fig. 11** Explosive dispersal of 5,100 kg gasoline: liquid fracture, fragmentation and jet formation

of primary jets. Yet small-scale experiments have been difficult in distinguishing the various jetting phenomena and their associated origins.

In order to clearly observe and understand the jet structures and their formation mechanism, the explosive dispersal from the large-scale experiment described in Sect. 2 is examined, whereby the test employed the same cylindrical charge configuration comprising a central burster of explosive surrounded by an annular gasoline payload. Figure 11 shows the high-speed photographic records for the early dispersal of gasoline payload.

After expanding to 1.5–2 times the initial diameter, the polyethylene casing begins to rupture longitudinally along the casing length (see photos at 1.5–2.5 ms in Fig. 11). At the same time, fine disturbances can be identified on the entire surface of the casing and develop into fine fragments followed by fine liquid jets (see photos at 2.5–4.5 ms). Radial fractures of the bulk liquid behind the longitudinal casing ruptures can be observed and become more visible after 4.5 ms. Primary spray jet structures develop between these radial fractures, much like in a "two-dimensional" fashion with a height matching the original burster explosive length for a considerable time (see the photos from 8 to 27 ms), while fine spray jets overlap these primary jet structures. From the front view of the last photo, ten primary jet structures are visible, correlated with the nine initial radial fractures of the liquid in the half circumference. In accordance with small-scale experiments, the circumferential number of fine jets decreases from its initial value as time progresses, while the primary jet number persists with a coherent jet structure.

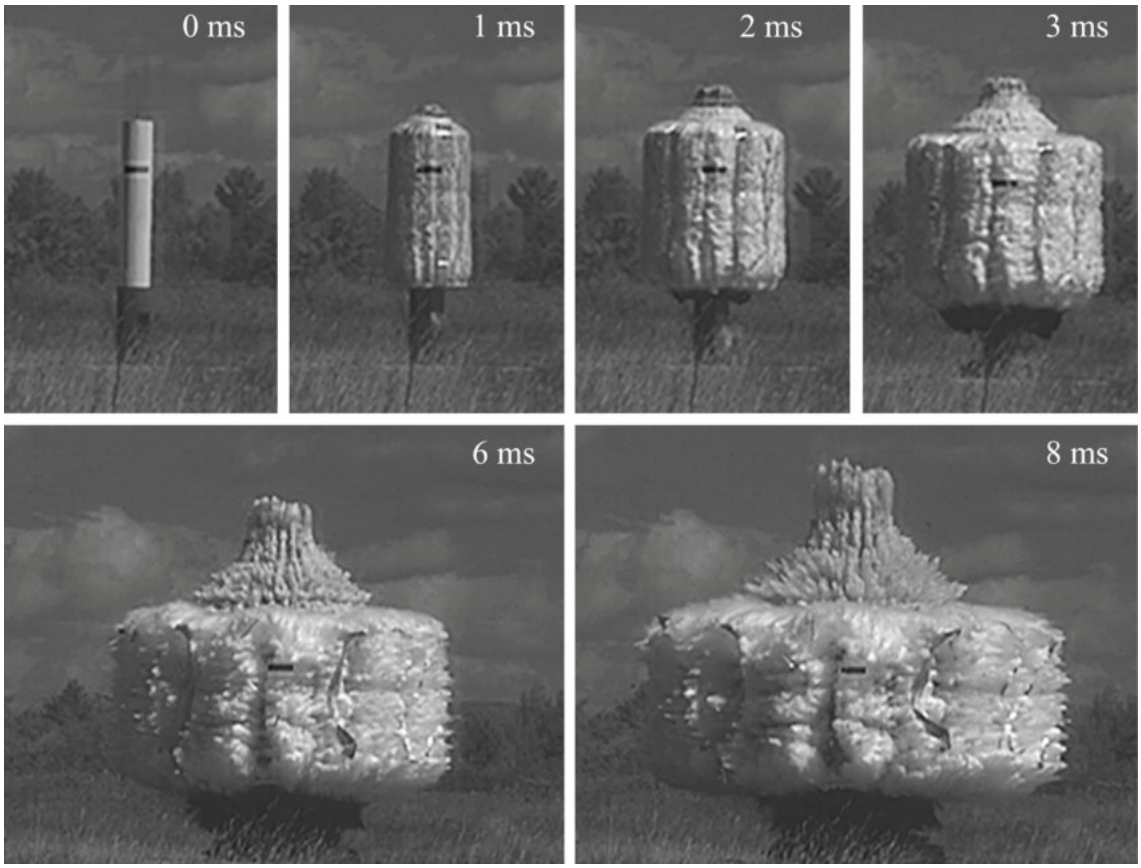


**Fig. 12** Early cylindrical explosive dispersal of 116 kg water in 30 cm ID and 1.65 m long thin-walled aluminum casing by a central burster of 1 kg explosive in a 25.4 mm ID thin-walled steel tube

The two-dimensional nature of the incipient occurrence of near-surface payload radial fractures aligned with longitudinal ruptures of the outer casing is more clearly displayed in a long cylindrical stratified charge configuration, consisting of a 116 kg water payload surrounding a 1 kg central explosive burster, as shown in Fig. 12. Here the water payload is contained in a 1.65 m long, 30 cm internal diameter (ID), thin-walled aluminum casing while the burster explosive is in a 25.4 mm ID thin-walled steel tube, itself concentrically located within the larger aluminum casing. Again, primary jets emerge between the fractures; from the front view of the photos six primary jet structures are visible, correlated with five initial radial fractures of the liquid in the half circumference.

Comparing the 2 L liquid charge using a 10 mm burster shown in Sect. 3.1 with the current two large charges, 116 kg water and 5,090 kg gasoline, the number of primary jets are 9, 10 and 18, respectively (assuming circumferential symmetry for the latter two). While the three charges possess a similar Gurney velocity, their burster casing materials are different. Hence, the number of primary jets depends not only on the mass ratio *M/C* as discussed in Sect. 3.1, but also on the dynamic response and fragmentation of burster casing materials. A scaling study would be necessary under the condition of same charge configuration and casing materials in order to determine the dependence of the number of primary jets on *M/C*.

In summary, a dual hierarchical jet structure consisting of primary jets overlapped by fine jets is clearly evidenced in the large-scale experiments. A large number of fine droplet jets form as the surface instabilities or fragmentation of the charge casing takes place. The number of these initial jets can be explained by the charge casing fragmentation theory as was done for the small-scale tests. At the same time, the near-surface liquid radial fractures are aligned with the initial longitudinal ruptures of the charge casing (i.e., not the fine casing fragments, rather the long vertical strips). The primary droplet jets then emerge between these fractures and the number of primary jets is therefore consistent with the fracture number. The fine jet instabilities overlap or merge on the surface of the primary jet structures as they are moving outwards.

Since the longitudinal ruptures of the charge casing incipiently occur with the radial fractures of near-surface liquid in a length consistent with the explosive burster, one would postulate that the radial liquid fractures could start from the

interior payload or the formation of primary jets must take place before the outer surface fine jets. It can therefore be suggested that the mechanism for the primary jet formation, born from near-surface liquid radial fractures, finds its origin in detonation-induced instability of the interior interface between burster explosive and the bulk liquid payload. The existence of a thin-walled interior casing containing burster explosive could further enhance or dominate this interface instability, where the fragment number of the interior casing may dictate the number of primary jets.

### 3.3 Numerical simulation

Macro-scale numerical modeling has been conducted to simulate the experimental observations and validate the mechanism postulated. The simulation modeled a small-scaled cylindrical charge 100 mm in diameter containing water ($\rho = 1\,\mathrm{g/cm^3}$) with a 10 mm diameter central burster of TNT ($\rho = 1.6\,\mathrm{g/cm^3}$). As experimentally observed, natural fragmentation of the payload outer casing usually led to incipient fine jets following the scales of fragments. When a metal outer casing was scored to promote tailored fracture, there were payload jets observed travelling in the wake of scored casing fragments for a long time; the jet cross-sections, however, were on the order of the areas of outer casing fragments. Those wake-induced jets did not have the scale of the primary jets nor their emergence process. The detailed numerical models for outer casing effects would form a subject for future study. In the present modeling, the interior explosive-liquid interface featured a thin pre-fragmented casing (steel, 0.9 mm thick), while the outer liquid-air boundary had no casing in order to demonstrate the mechanism without the influence of an outer casing.

A two-dimensional planar domain was used to represent the cross-section of a long cylindrical charge, while symmetry planes were employed to represent one-quarter of the charge circumference to maximize both numerical resolution and efficiency for given resources. The explosive was centrally initiated with a cylindrical detonation propagating outwards. The early shock dynamics, including detonation and shock transmission into the bulk liquid, was calculated on a Eulerian mesh using continuum material models. The TNT burster was represented by a Mie-Grüneisen equation of state (EOS) and the Jones–Wilkins–Lee (JWL) EOS was used for its detonation products. The Tait EOS was used for the water in compression followed by an isentrope under small tension. A closely-coupled fluid-structure interaction capability was used for the burster casing fragments in which a conservative locally-adaptive mesh approach was used. The CFD mesh was unstructured quadrilateral elements 0.2 mm in size; the casing structural elements were also 0.2 mm. Within the quarter-symmetric model, the burster casing was pre-failed at four equally-spaced points, representing 16 fragments around the entire circumference under a symmetry assumption. Equal-sized fragments were chosen as a starting point in the absence of an experimental fragment size distribution and to avoid uncertainty in the material and failure models required for simulating natural fragmentation. The fragment number used in the numerical calculations was selected within the range of the number of primary jets in the 2 L liquid dispersal tests.

Breakup of the bulk liquid is a complex process and was not simulated in detail. Instead, a simple cavitation damage model was used, assuming instantaneous fragmentation upon the appearance of a local tensile condition whereby the continuum density matched dense-packed spheres separated by vapor [21]. Thus the breakup criterion was essentially strain-based for the bulk liquid expansion corresponding to a pressure of 5,000 Pa, equivalent to a tensile strain of 0.006. At the instant of breakup, the liquid was converted from Eulerian to Lagrangian 'particle' groups while mass conservation was ensured with the vapor remaining in the gas phase.

The droplet sizes were many orders of magnitude less than the cloud scale formed by explosive dispersal and were not resolved in the measurements. For modeling purposes, the initial sizes were assumed to follow a normal distribution within the bounds predicted by Grady's spall theory and viscous dissipation mechanism with parameters for water [19]. The Lagrangian 'particle' group method was designed to represent a range of particle diameters spanning several orders of magnitude in size. Within a 'particle' group, the number of physical droplets was constant (15,754 for each group used in the current calculation) and their diameters were the same. While the normal size distribution covers droplet particle sizes of 26–307 μm, the majority of droplets had a mean size of 120 μm. The denser liquid compressed by the detonation products was later fragmented at a fixed time of 50 μs into a normal size distribution ranging from 58 to 490 μm with a mean of 250 μm. In this calculation, a total of 210,519 Lagrangian groups were created and therefore the size distribution of groups was representative of the total distribution of physical droplets ($3.317 \times 10^9$ in number). The 'particle' dynamics were computed using a simple drag law as a function of Reynolds number alone. A series of remapping steps were performed on successively larger meshes, with the resolution from the initial 0.2 mm mesh size to final being 60 mm at 15 m radius. The above capabilities have been implemented in the Chinook CFD code developed by Martec Limited and Defence Research and Development Canada [22]. The numerical results also provided information on local mixture of droplets and vapor as well as their concentrations which can be used to assess detonability.

The mesh dependency of numerical calculations has been examined through a refined mesh with double the resolution (0.1 mm in initial cell size) for the same problem. The number of Lagrange droplet groups was correspondingly increased

to 739,289. The outer surface perturbations without a casing were expected to be dependent on the mesh resolution and the results showed that the perturbations were better resolved on the high resolution. In contrast, the interior perturbations depended on the pre-described number of burster fragments and the results provided the same number of interior perturbations for both mesh resolutions, thus indicating the independence of the interior perturbation number on mesh resolution. The selected mesh resolution is therefore justified, considering that the numerical calculations are focused to investigate the origins of the primary jets and their number in association with the interior interface perturbations.

Figure 13 displays the numerical results. As the explosive detonation reaches the surface of the burster casing, the five casing fragments start to move outwards within the quarter-symmetrical domain. The shock in water reaches the outer boundary (air interface) and reflects as an expansion wave travelling inwards; at 30 μs the transmitted air shock front is located at $R_s = 0.0587$ m. Due to its inertia a fragment moves faster than the neighboring liquid and is therefore followed by a high-pressure detonation products gas jet, the latter of which thus results in a surrounding compressed liquid strip or a cumulative 'ρ-layer' (Fig. 13 at 50 μs, where the air shock at $R_s = 0.0744$ m is undistinguishable). At this moment the fragments have a velocity >650 m/s while the velocity of the neighboring liquid at the same radius is about 250–300 m/s. The high-pressure gas jets behind the fragments therefore squeeze the liquid between them. The ρ-layer leading edges in front of the five fragments exhibit the highest circumferential strain, thus resulting in the first liquid failure or becoming fracture points near the outer surface as the fragments move outwards. In the meantime, the four squeezed filaments of the ρ-layer between these fracture points accelerate, marked as arrows in Fig. 13, while most of the liquid breaks into droplet particles due to tensile stresses (Fig. 13 at 4 ms, air shock at $R_s = 1.91$ m). At this time, many fine jets are visible on the surface and make the near-surface radial fracture points less visible. The fine jets appear to originate as a liquid-air surface instability. The small surface disturbance affects the timing of the local liquid breakup and therefore some droplet groups are formed slightly earlier than others. The droplets formed near the surface inherit this small disturbance with a gradient of momentum, leading to the growth of the fine jets on the surface. Note that grid resolution can also affect this surface instability without a casing, with an increase in perturbation number towards higher resolutions, appearing somewhat like particle streaks. This mesh effect was minimized by choosing a finer grid resolution than the surface instability scale.

Now, due to their higher velocity (i.e., higher momentum), the four squeezed particle filaments move faster than and eventually overtake the discrete particles in the neighboring gas jets downstream of the fragments, as evidenced in Fig. 13 at 10 ms (air shock at $R_s = 4.32$ m). This finally leads to the emergence of the primary particle jets out of the surface of fine jet perturbations. Within the quarter-symmetric model, four primary particle jets are developed between the five liquid fracture points and are thus correlated to the five fragments of the interior burster casing.

The mass of each primary particle jet largely depends on the mass of the corresponding compressed filament, which would be related to the fragment cross-section area normal to the radial direction. For instance, the second fragment in the counter-clockwise order rotates by asymmetric forces, resulting in a small cross-section area (see Fig. 13 from 10 to 50 μs). This causes a narrower high-pressure gas jet behind and subsequently a larger mass of neighboring liquid filament, leading to a larger mass of primary particle jet.

In order to further distinguish the primary jets from fine jets and to study the influence of the mass ratio of payload to explosive, $M/C$, for a given fragment size, the explosive burster diameter is scaled up from 10 to 20 mm without any other changes to the charge. This results in a decrease in $M/C$, thus increasing the incipient expansion velocity as depicted in Fig. 9. In this case, the burster casing is pre-failed at eight equally-spaced points within the quarter-symmetric model, representing 32 fragments with the same size as before around the entire circumference. Figure 14 shows that eight compressed filaments are formed following a compressed layer and that the filament number is controlled by the nine fragments of the interior burster casing (see $t = 0.04$–1 ms). The higher speed of filament particles then leads to the emergence of eight primary particle jets ($t = 10$–100 ms) between the nine near-surface liquid radial fracture points. When compared to Fig. 13, the primary particle jets emerge sooner out of the surface of fine jet perturbations and become more coherent and dominant (e.g., at 100 ms, the finer or thinner jets are much less visible between adjacent primary jets) with a decrease in $M/C$. In other words, as the charge surface expansion velocity decreases to a critical limit with an increase in $M/C$, the circumferential strain of the most stretched payload front edges remains below the fracture failure criterion. In this case, the primary jets will not develop and emerge, but rather dissipate within the payload comprising a large $M/C$.

The dissipation of primary jets by large $M/C$, whereby the jets are induced from the interior interface instability, can be simulated using smaller inner casing fragments. Figure 15 shows the calculation using the 20 mm diameter burster, with its casing pre-failed into 32 fragments in a period of every three 2.45 mm sized followed by one 0.49 mm sized fragment (instead of all 1.96 mm equal-sized fragments in the previous two calculations). This calculation employed 406,655 Lagrange groups representing $3.233 \times 10^9$ droplets, with an average of 7,950 physical droplets per Lagrange group. Within the quarter-symmetrical domain, there are nine

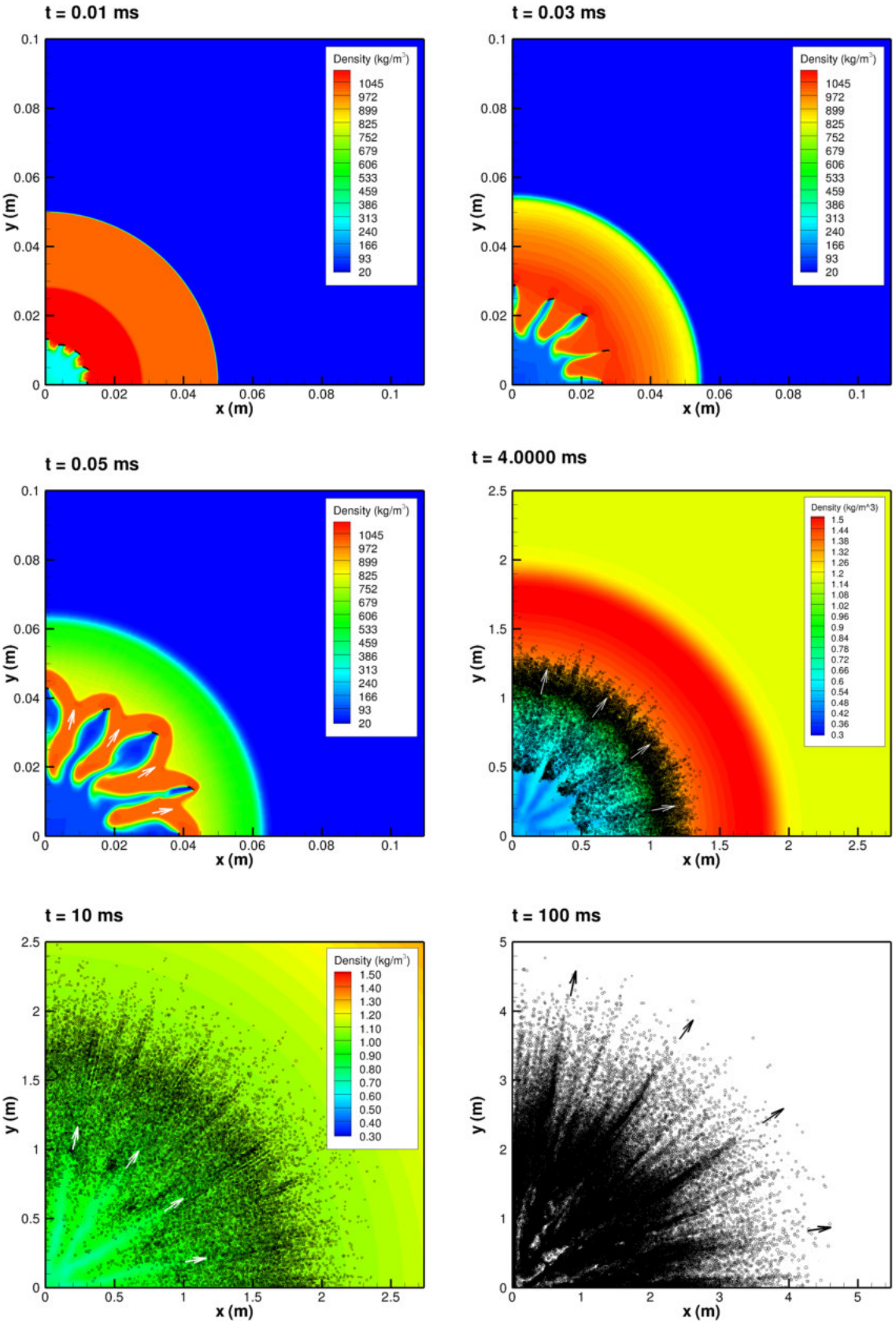


**Fig. 13** Liquid dispersal: fracture, fragmentation and jet formation using a 10 mm dia. burster, with its casing pre-failed into 16 pieces of 1.96 mm sized fragments

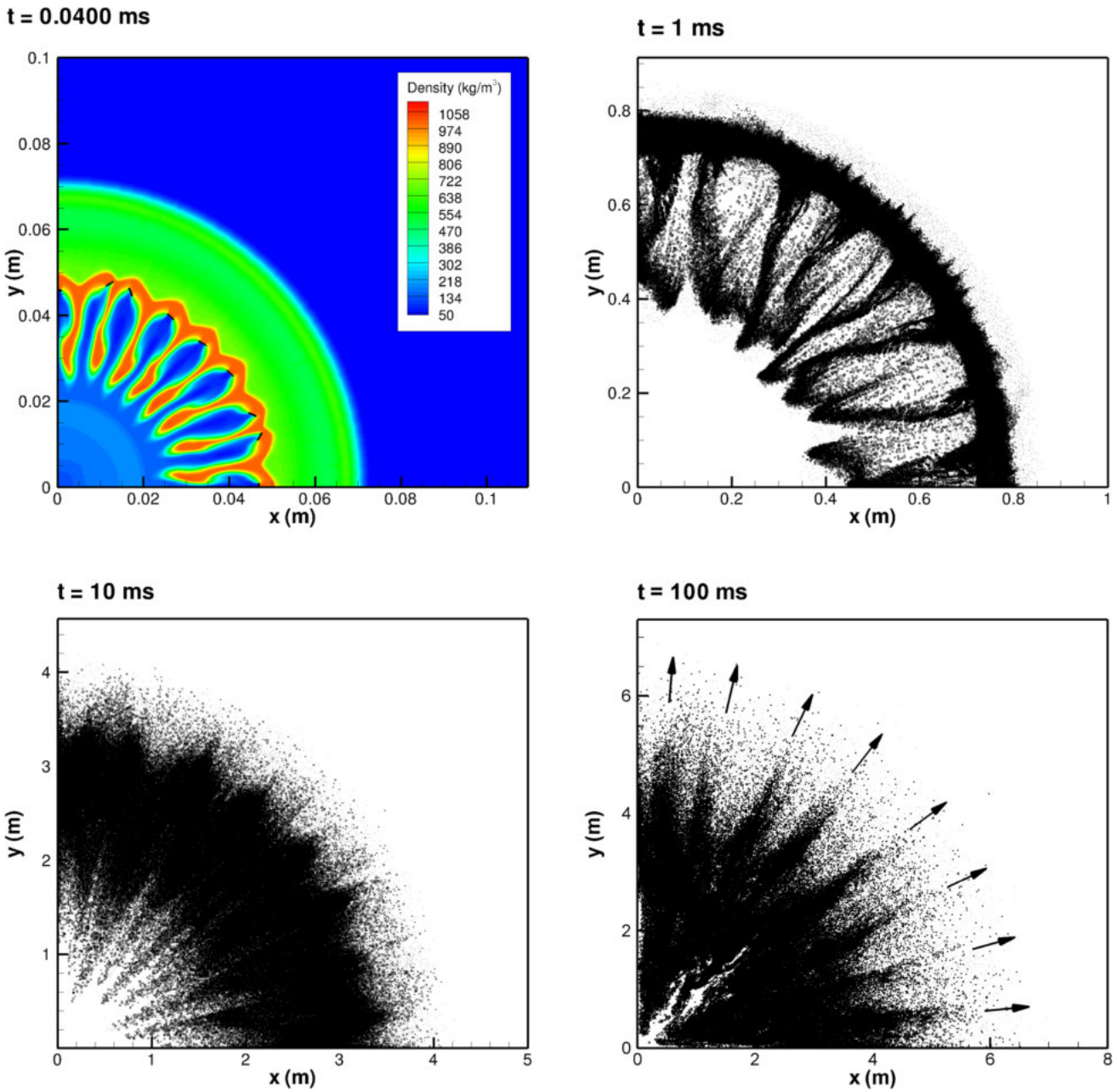


**Fig. 14** Liquid dispersal: fracture, fragmentation and jet formation using a 20 mm dia. burster, with its casing pre-failed into 32 pieces of 1.96 mm sized fragments

casing fragments, two of which are 0.49 mm in size. The detonation products gas jets downstream of the two 0.49 mm fragments are weaker than those behind the seven larger fragments (Fig 15 at 20 μs, air shock at $R_s = 0.0556$ m). The two weaker gas jets dissipate through the liquid payload ahead during expansion and the compressed liquid strips are subsequently degenerated into six filaments, leading to the emerging of six primary particle jets later in time. Thus, for a given fragment size, there is a critical *M/C* beyond which primary jets will not develop. When compared to Fig. 14, for a given *M/C* a critical fragment size lies between 1.96 and 0.49 mm for the dissipation of primary jets.

From the above computations, the number of primary particle jets emerging between the near-surface liquid radial fracture points can be traced back to the number of compressed liquid filaments, which is determined by the fragment number of the interior casing between the burster explosive and the bulk liquid. The number of filaments right before liquid surface bursting further depends on *M/C* and inner casing fragment pattern, whereby the jets induced by minor frag-

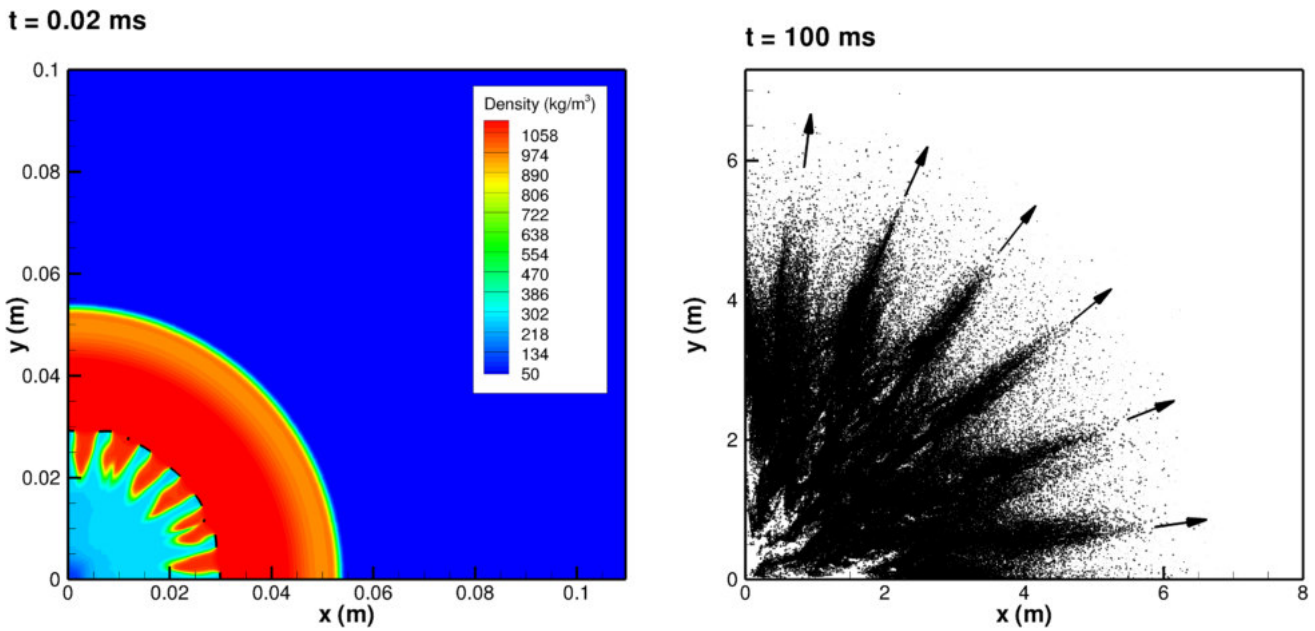


**Fig. 15** Numerical results for the same configuration as shown in Fig. 14, but with its inner casing pre-failed into 32 fragments in a period of every three 2.45 mm sized followed by one 0.49 mm sized fragment

ments will dissipate and not result in final filaments. While the numerical models need further quantitative improvements, the simulations are qualitatively in agreement with the experimental observation about the consistency of primary particle jet number with the near-surface payload radial fractures. The numerical results further depict in detail that the formation of the fractures and primary particle jets is due to the development of compressed payload filaments that originate in the interfacial instabilities between explosive and payload, thus verifying the postulated mechanism.

## 4 Conclusion

A large-scale experiment involving unconfined detonation of a 5,090 kg gasoline spray in air has been successfully conducted through the explosive dispersal of a cylindrically stratified charge configuration. The detonation observed has a mean velocity of 1,890 m/s and a pressure ratio range of 18.0–24.5, with a mean detonation cell width of approximately 7 cm. Explosive dispersal of bulk gasoline liquid leads to the formation of a spray cloud consisting of a number of particle jet structures that remain coherent after travelling for many charge diameters.

Clustering and jetting structures are a fundamental phenomenon observed in the explosive dispersal of a payload, consisting of either a bulk liquid, granular materials or a mixture of both. For a liquid payload packed in a stratified shell surrounding an explosive, the present paper explores a dual jetting instability hierarchy based on the observation from large-scale experiments and a careful revisit of previous small-scale experiments. The dual hierarchical jet structure consists of primary droplet or particle jet structures overlapped by numerous fine jets on the primary surfaces. While both jet systems develop very early within the expansion of 1.5–2 times the initial charge diameter, the primary jets emerge out of the surface of fine jet structures later in time. The primary jet number is consistent with the number of radial fractures near the payload surface. Based on the experimental observation, a physical mechanism for the dual jet structure is proposed: the primary jet structures originate in the interior boundary between the explosive and the payload, while the fine jet instabilities are formed at the outside boundary between the payload and air. In practice, each interface may feature a thin casing material that breaks up, thereby enhancing or likely dominating the instabilities, respectively.

If the inner casing containing the explosive is assumed to fragment into a number of fragments, numerical modeling results in the subsequent formation of a similar number of primary jets, consistent with the experimental observation. The numerical results further demonstrate that the high-pressure jets of detonation products, created from the interior casing fragmentation, radially fracture the payload. The resulting compressed radial filaments, developed within the payload, lead to the primary jets emerging between the radial fracture points on the payload surface. The number of primary particle jets is therefore determined by the number of compressed payload filaments before payload surface bursting. The number of payload filaments depends on the number of neighboring high-pressure detonation product jets which follow the

fragments of the inner explosive casing, but also depends on mass ratio of payload to explosive and inner casing fragment pattern. The detonation product jets induced by minor fragments may dissipate through large payload and therefore not result in final filaments. The numerical simulations are therefore in agreement with the postulated mechanism that the formation of the primary particle jets originates in the perturbations that develop near the interior interface between explosive and payload, either through casing fragmentation or other non-uniform density effects, driven by the explosive detonation and subsequent expansion of the high-pressure detonation products.

The mechanism investigated in the current paper addresses the importance of instabilities from non-uniform density effects near the interior interface for particle clustering and jetting through bulk liquid dispersal. Explosive dispersal of granular materials is more complicated due to additional physical effects originating in the nature of discrete grain-scale solids. The instabilities from non-uniform density effects near an interior explosive interface and their interactions with bulk deformable and compressible materials may still contribute to the clustering and jetting in granular material dispersal in a stratified shell configuration. An example for the non-uniform density effects similar to the interior casing fragments would include agglomerates through shock compaction and sintering near the explosive interface. A thorough understanding of the effect of such instabilities is therefore important in the quantitative description of the clustering and jetting phenomenon for both bulk and granular materials.

**Acknowledgments** The significant effort and support of Brian Eichelbaum, Kiril Mudri, Robin Laing, Darrell Boechler, Karl Baker, the technical staff from the Suffield Field Operations Section and Richard Guilbeault from Canadian Explosive Research Laboratory in conducting the experiments, and Chris Cloney and Scott McClennan for the numerical model development are gratefully acknowledged. The research reported herein was supported by Defence Research and Development Canada (DRDC) and the US Defense Threat Reduction Agency (DTRA)—Advanced Energetic Program (Dr. William H. Wilson).

## References

1. Alekseev, V.I., Dorofeev, S.B., Sidorov, V.P., Chaivanov, B.B.: Experimental study of large-scale unconfined fuel spray detonations. Prog. Astronaut. Aeronaut. **154**, 95–104 (1993)
2. Alekseev V.I., Dorofeev, S.B., Sidorov, V.P.: Direct initiation of detonations in unconfined gasoline sprays. Shock Waves **6**, 67–71 (1996)
3. Dorofeev, S.B.: Blast effects of confined and unconfined explosions. In: Sturtevant, B., Shepherd, J.E., Horning, H.G. (eds.) Proceedings of the 20th International Symposium on Shock Waves, July 1995, pp. 77–86. World Scientific, Pasadena, CA (1995)
4. Dorofeev, S.B., Sidorov, V.P., Kuznetsov, M.S., Dvoinishnikov, A.E., Alekseev, V.I., Efimenko, A.A.: Air blast and heat radiation from fuel-rich mixture detonations. Shock Waves **6**, 21–28 (1996)
5. Zhang, F., Gerrard, K., Ripley, R.C.: Reaction mechanism of aluminum particle-air detonation. J. Propul. Power **25**(4), 845–858 (2009)
6. Frost, D., Zhang, F.: The nature of heterogeneous blast explosives. In: Proceedings of the 19th International Symposium on Military Aspects of Blast and Shock, 1–6 October 2006, Calgary, Canada (2006)
7. Ritzel, D.V., Ripley, R.C., Murray, S.B., Anderson, J.: Near-field blast phenomenology of thermobaric explosions. In: Hannemann, K., Seiler, F. (eds.) Proceedings of the 26th International Symposium on Shock Waves, 15–20 July 2007, pp. 281–286. Springer, Göttingen (2007)
8. Zhang F., Yoshinaka A., Ripley R.: Hybrid detonation waves in metalized explosive mixtures. In: Proceedings of the 14th International Detonation Symposium, 11–16 April 2010, pp. 714–723. Office of Naval Research, Coeur d'Alene, Idaho (2010)
9. Milne A.M., Parrish C., Worland, I.: Dynamic fragmentation of blast mitigants. Shock Waves **20**, 41–51 (2010)
10. Frost, D.L., Grégoire, Y., Goroshin, S., Zhang, F.: Interfacial instabilities in explosive gas-particle flows. In: Proceedings of the 23rd International Colloquium on the Dynamics of Explosion and Reactive Systems (ICDERS), 24–29 July 2011, Irvine, CA (2011)
11. Ripley, R.C., Donahue, L., Zhang, F.: Jetting instabilities of particles from explosive dispersal. In: Proceedings of the 17th International Conference of Shock Compression of Condensed Matter, 26 June–1 July 2011, pp. 1615–1618. American Institute of Physics, Chicago, IL (2011)
12. Zhang, F.: Metalized heterogeneous detonation and dense reactive flow – plenary lecture. In: Proceedings of the 17th International Conference of Shock Compression of Condensed Matter, 26 June–1 July 2011, pp. 25–32. American Institute of Physics, Chicago, IL (2011)
13. Xu, T., Lien, F.-S., Ji. H., Zhang, F.: Formation of particle jetting in a cylindrical shock tube. Shock Waves **24**, 537–553 (2013)
14. Ripley, R.C., Zhang, F.: Jet instability mechanisms of particles from explosive dispersal. In: Proceedings of the 18th International Conference of Shock Compression of Condensed Matter, 7–12 July 2013. American Institute of Physics, Seattle, WA (2013)
15. Gauss, A.: Fuel and hydrocarbon vaporization. AD-769709, Ballistic Research Laboratories, Aberdeen Proving Ground, MA (1973)
16. Bastea, S., Fried, L.E.: Chemical equilibrium detonation. In: Zhang, F. (ed) Detonation Dynamics, pp. 1–31. Springer, Heidelberg (2012)
17. Knystautas, R., Guirao, C., Lee, J.H., Sulmistras, A.: Measurements of cell size in hydrocarbon-air mixtures and predictions of critical tube diameter, critical initiation energy, and detonability limits. Prog. Astronaut. Aeronaut. **94**, 23–37 (1984)
18. Meyers, M.A.: Dynamic behavior of materials, pp. 234–242. Wiley, New York (1994)
19. Grady, D.E.: The spall strength of condensed matter. J. Mech. Phys. Solids **36**(3), 353–384 (1988)
20. Grady, D.: Fragmentation of rings and shells. Springer, Heidelberg (2006)
21. Kedrinskii, V. K.: Hydrodynamics of Explosion. Springer, Heidelberg (2005).
22. Chinook code software manual #SM-13-06 Rev 22, 1 March 2013, Martec Limited, Halifax, NS, Canada (2013)